

# Composition dependence of magnetic properties in perpendicularly magnetized epitaxial thin films of Mn-Ga alloys

S. Mizukami, T. Kubota, F. Wu, X. Zhang, and T. Miyazaki

*WPI-Advanced Institute for Materials Research, Tohoku University, Sendai 980-8577, Japan*

H. Naganuma, M. Oogane, A. Sakuma, and Y. Ando

*Department of Applied Physics, Tohoku University, Sendai 980-8579, Japan*

(Received 5 August 2011; revised manuscript received 17 December 2011; published 18 January 2012)

Mn-Ga binary alloys show strong magnetism and large uniaxial magnetic anisotropy even though these alloys do not contain any noble, rare-earth metals or magnetic elements. We investigate the composition dependence of saturation magnetization  $M_S$  and uniaxial magnetic anisotropy  $K_u$  in epitaxial films of  $\text{Mn}_x\text{Ga}_{1-x}$  alloys ( $x \sim 0.5-0.75$ ) grown by magnetron sputtering. The  $M_S$  values decrease linearly from approximately 600 to 200 emu/cm<sup>3</sup> with increasing  $x$ , whereas the  $K_u$  values decrease slightly from approximately 15 to 10 Merg/cm<sup>3</sup> with increasing  $x$ . These trends are distinct from those for known tetragonal hard magnets obtained in a limited composition range in Mn-Al and Fe-Pt binary alloys. These data are analyzed using a localized magnetic moment model.

DOI: [10.1103/PhysRevB.85.014416](https://doi.org/10.1103/PhysRevB.85.014416)

PACS number(s): 75.20.Hr, 73.61.At, 75.30.Gw, 75.70.Ak

## I. INTRODUCTION

The demand for perpendicular magnetization films has increased considerably since these films are crucial in advanced spintronics applications, such as high-density perpendicular magnetic recording and Gbit-class spin-transfer-torque magnetic random access memory (STT-MRAM).<sup>1-3</sup> As sizes of magnets are reduced to several tens of nm to increase storage densities in these applications, thermal fluctuations in the magnetization direction become substantial, thereby causing memory loss in such storage devices. A high magnetic anisotropy of over 10 Merg/cm<sup>3</sup> is required in practice to maintain the magnetization direction in such nanoscale magnets, and therefore, a variety of perpendicular magnetization films has been investigated thus far. Mn-Ga binary alloys are similar to Mn-Al binary alloys in the sense that they are hard magnets. Both these alloy types show strong magnetism even though they consist of nonmagnetic and light elements. Despite Mn-Ga alloys exhibiting strong magnetism over a much wider compositional range when compared with Mn-Al alloys, the former have been studied less extensively.

Alloys of Mn-Ga with  $L1_0$  structure are thermodynamically stable for  $x \sim 0.5-0.65$  [Fig. 1(a)].<sup>4</sup> Although magnetization decreases as the Mn composition  $x$  increases, these alloys have a large magnetic anisotropy with magnetically easy axis parallel to the  $c$  axis.<sup>4</sup> In the past decade, several groups have investigated the structural, magnetic, and transport properties for off-stoichiometric  $L1_0$  Mn-Ga films with a view to their magneto-optical and spintronics applications.<sup>5-8</sup> For  $x \sim 0.65-0.75$ , the  $D0_{22}$  structure appears to exhibit strong *ferrimagnetism* [Fig. 1(b)], as confirmed by neutron scattering.<sup>9</sup> A high Curie temperature of up to  $\sim 800$  K, large magnetic anisotropy, and composition-sensitive magnetization were also reported in  $D0_{22}$ -phase polycrystalline bulk samples.<sup>10</sup>

Recently, renewed interest in  $D0_{22}$   $\text{Mn}_3\text{Ga}$  has been expressed in the context of Heusler alloys because the  $D0_{22}$  structure can be depicted as a tetragonally distorted  $D0_3$

structure that is similar to the  $L2_1$  structure in Heusler alloys. In the case of  $D0_3$   $\text{Mn}_3\text{Ga}$  that is not stable in reality, the band structure calculated from first principles exhibits a spin polarization close to unity, namely that of a half metal.<sup>11,12</sup> Tetragonally distorted  $D0_{22}$   $\text{Mn}_3\text{Ga}$  is not a half metal; however, it still exhibits a spin polarization as large as 88%, as predicted by the calculation from first principles.<sup>13</sup> The structural and magnetic properties of bulk  $D0_{22}$  Mn-Ga alloys with off-stoichiometric compositions have been investigated, and the results suggest that vacancies produced by Mn deficiencies increase the magnetic moment significantly in the  $D0_{22}$  phase.<sup>14</sup>

We have recently reported on  $c$ -axis-oriented, off-stoichiometric  $D0_{22}$   $\text{Mn}_{2.5}\text{Ga}$  epitaxial films, prepared by the sputtering technique, that exhibited a uniaxial perpendicular magnetic anisotropy constant  $K_u$  of over 10 Merg/cm<sup>3</sup>.<sup>15-17</sup> Moreover, the Gilbert damping constant, which determines the critical current density for STT switching, was smaller for Mn-Ga alloy films with  $D0_{22}$  or  $L1_0$  phases than for the perpendicularly magnetized films previously reported.<sup>18</sup> In addition, we also predicted the presence of large tunnel magnetoresistance (TMR) effect of over 600% in MgO-based  $D0_{22}$   $\text{Mn}_3\text{Ga}$  magnetic tunnel junctions (MTJs).<sup>19</sup> The experimental TMR ratio in a  $D0_{22}$ - $\text{Mn}_{2.4}\text{Ga}/\text{MgO}/\text{CoFe}$  MTJ was 22.1% at 10 K,<sup>19,20</sup> even though the experimental spin polarization estimated by using a point contact Andreev reflection was as high as 58%.<sup>21</sup> Large perpendicular magnetic anisotropy, small damping constant, and large TMR ratio are important requirements for STT-MRAM;<sup>2,3</sup> consequently, Mn-Ga alloys may be one of the key materials for this type of application.

Several groups have recently reported the structural and magnetic properties of Mn-Ga alloy films with  $D0_{22}$ -ordered<sup>22,23</sup> or  $L1_0$ -ordered<sup>24-27</sup> structures. These reports focused on the limited composition range belonging to  $D0_{22}$  or  $L1_0$  phases. Further, it is noteworthy that all previous studies on compositional dependence have been performed with polycrystalline bulk samples, and consequently, it has thus far been difficult to estimate exact values for  $M_s$  and

particularly  $K_u$  against varying Mn composition because of the exceedingly large saturation fields involved.<sup>4,10,14</sup> Recent studies have reported the composition dependence of the TMR ratio in MgO-based Mn-Ga MTJ.<sup>28</sup> In this study, we report the wide-range composition dependence of  $M_s$  and  $K_u$  in thin epitaxial films of Mn-Ga alloys, and we discuss these dependencies using a localized magnetic moment model.

## II. EXPERIMENTAL AND COMPUTATIONAL PROCEDURES

In our experiment, 30-nm-thick  $\text{Mn}_x\text{Ga}_{1-x}$  films were deposited on Cr-buffered single-crystal (100) MgO substrates under an Ar pressure of 0.1 Pa using magnetron sputtering with a base pressure of less than  $10^{-6}$  Pa. We prepared alloys films with  $x = 0.54, 0.62,$  and  $0.72$  using Mn-Ga alloy targets of different compositions, and the films with  $x = 0.65$  and  $0.75$  were prepared using the co-sputtering technique. Films with  $x = 0.75$  were grown at a substrate temperature of  $400^\circ\text{C}$  because the stoichiometric  $\text{Mn}_3\text{Ga}$  films were not available on a Cr buffer after a postannealing procedure. Films with other compositions were grown at room temperature and subsequently annealed at  $400\text{--}500^\circ\text{C}$  *in situ*. After cooling to room temperature, all the films were capped with a Ta layer to prevent oxidation.

The composition of the Mn-Ga films was carefully analyzed several times by inductively coupled plasma mass spectrometry. Structural analysis was performed by using an out-of-plane and in-plane x-ray diffractometer (XRD) with a 9-kW rotating anode, and the Cu  $K_\alpha$  line was used for the analysis. Magnetization measurements were carried out using a vibrating sample magnetometer as well as a superconducting quantum interference device magnetometer.

The electronic band structures of  $L1_0$ -ordered MnGa and  $D0_{22}$ -ordered  $\text{Mn}_3\text{Ga}$  were calculated with linear muffin-tin orbitals in the atomic sphere approximation (LMTO-ASA) based on the density functional formalism. To calculate the  $K_u$  values, we used LMTO-ASA including the spin-orbit interaction and the force theorem.<sup>18,29,30</sup>

## III. EXPERIMENTAL RESULTS

Figure 2 shows examples of the XRD patterns obtained for 30-nm-thick  $\text{Mn}_x\text{Ga}_{1-x}$  alloy films deposited on a Cr buffer layer. The XRD patterns showed only the sharp (002) and (004) diffraction peaks for these films; the other diffraction peaks correspond to the substrate. The (002) and (004) diffraction peaks are respectively attributed to the superlattice peak for the  $L1_0$ -type ordering and the fundamental peak of the  $L1_0$  and  $D0_{22}$  Mn-Ga alloys for the unit cells shown in Figs. 1(a) and 1(b). From the XRD results, the  $\text{Mn}_x\text{Ga}_{1-x}$  alloy films appear to exhibit a single phase solid solution in the range of  $0.5 < x \leq 0.75$ , and this is consistent with the results reported for the bulk samples.<sup>10</sup> However, the (002) and (004) diffraction peaks for the alloy films became broader at  $x = 0.75$ , thereby indicating that the film structure is degraded when compared with those of alloy films with intermediate compositions.

Figure 3(a) shows the Mn concentration dependence of the lattice constants estimated from the XRD patterns for the alloy films. The in-plane lattice constant  $a$  is roughly

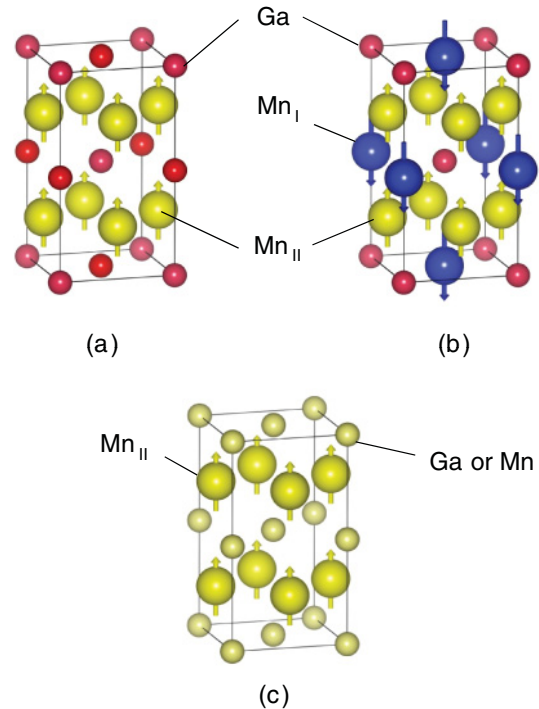


FIG. 1. (Color online) Schematic of a unit cell of crystal structure for (a)  $L1_0$ -ordered MnGa, (b)  $D0_{22}$ -ordered  $\text{Mn}_3\text{Ga}$ , and (c)  $\text{Mn}_x\text{Ga}_{1-x}$  ( $0.5 < x \leq 0.75$ ) alloys ordered maximally in the  $L1_0$  structure with no vacancies. The unit cell in (a) is doubled along the  $c$  axis for comparison with the  $D0_{22}$  unit cell. In (b), Mn atoms that occupy Wyckoff positions  $2b$  and  $4d$  are denoted by  $\text{Mn}_I$  and  $\text{Mn}_{II}$ , respectively; Ga atoms are located at the Wyckoff position  $2a$  (Ref. 14). The magnetic moment of  $\text{Mn}_I$  is antiparallel to that of  $\text{Mn}_{II}$ . The  $\text{Mn}_I$  atoms in the  $D0_{22}$  structure are replaced by Ga atoms in the  $L1_0$  structure. In (c), Ga and Mn atoms are randomly located at both  $2a$  and  $2b$  positions.

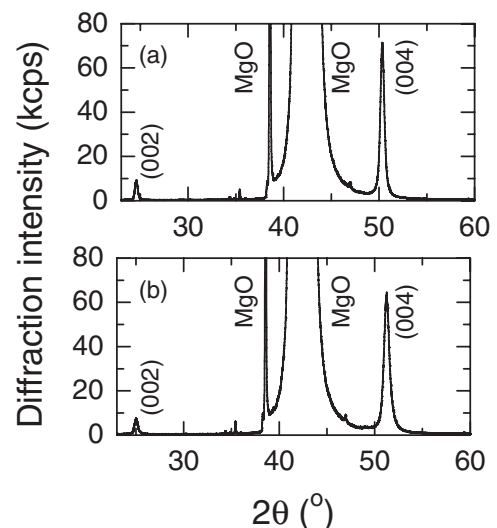


FIG. 2. Example of x-ray diffraction patterns for 30-nm-thick  $\text{Mn}_x\text{Ga}_{1-x}$  alloy films deposited on a Cr buffer layer. (a)  $x = 0.54$  and (b)  $x = 0.62$ .

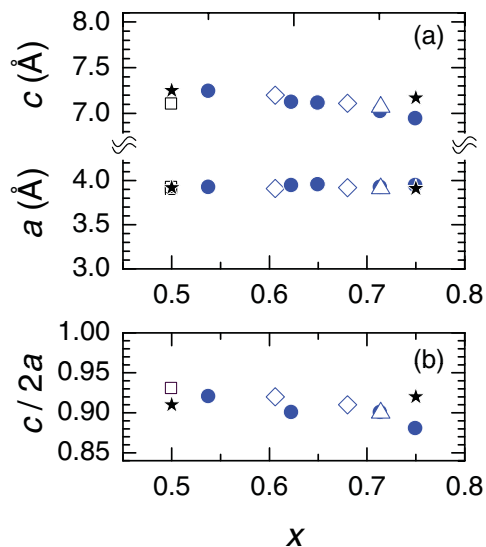


FIG. 3. (Color online) Composition dependence of (a) in-plane (out-of-plane) lattice constant  $a$  ( $c$ ) and (b) tetragonal distortion ratio  $c/2a$  for  $\text{Mn}_x\text{Ga}_{1-x}$  alloy films with thicknesses of 30 nm ( $\bullet$ ) and 100 nm ( $\Delta$ ) deposited on a Cr buffer layer (Ref. 15), and with thickness of 100 nm deposited on a MgO substrate ( $\diamond$ ) (Ref. 18). Values used in the first-principles calculations in Ref. 30 and in this report are represented by  $\square$  and  $\star$ , respectively. The  $c$  values in  $L1_0$  films are doubled, for comparison with those in  $D0_{22}$  films.

independent of  $x$ , whereas the out-of-plane lattice constant  $c$  decreases slightly with increasing  $x$ . Figure 3(b) shows the plot of the tetragonal distortion ratio  $c/2a$  as a function of  $x$ . Most of the alloy films show a  $c/2a$  ratio of 0.90–0.92. The magnitude of the quantities and the curve trends in Figs. 3(a) and 3(b) are comparable with those reported for bulk samples, thereby indicating good film quality.<sup>10</sup> The values for  $c$  and  $c/2a$  at  $x = 0.75$  are slightly different from those at other  $x$  values, probably owing to structural strains that may be related to an instability in the  $D0_{22}$  structure in the stoichiometric  $\text{Mn}_3\text{Ga}$ .<sup>10</sup>

Figure 4 shows examples of the hysteresis curves for 30-nm-thick  $\text{Mn}_x\text{Ga}_{1-x}$  alloy films deposited on a Cr buffer layer. The magnetization curves for all the films show rectangular shapes with a squareness close to unity if a magnetic field is applied perpendicular to the film plane; this enables us to evaluate the saturation magnetization  $M_S$ .

Figure 5(a) shows the  $x$  dependence of  $M_S$  for the alloy films. It is noteworthy that the value for  $M_S$  decreases very linearly and systematically from about 600 to 200  $\text{emu}/\text{cm}^3$  with increasing  $x$ . Most of the  $M_S$  values for our films are larger for any  $x$  values than those in previous reports; however, the  $M_S$  value for the  $\text{Mn}_2\text{Ga}$  films reported in Ref. 22 is slightly larger than that in our films, as shown in Fig. 5(a).

The values for  $K_u$  against  $x$  in the alloys films are also shown in Fig. 5(b). The  $K_u$  values are determined using the relation  $K_u = M_S H_k^{\text{eff}}/2 + 2\pi M_S^2$ , where  $H_k^{\text{eff}}$  denotes the effective magnetic anisotropy field estimated from the magnetization curves for measurements taken when the applied magnetic field is in the film plane. Although the values for  $K_u$  tend to be larger for films with lower Mn compositions and with large thicknesses, all the films show large  $K_u$  values

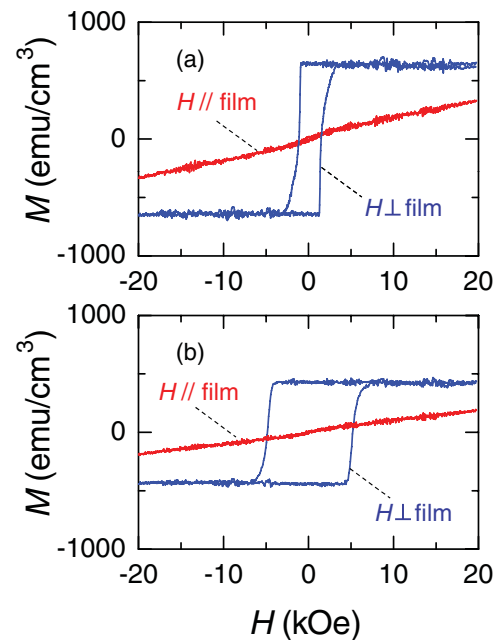


FIG. 4. (Color online) Example of hysteresis curves for 30-nm-thick  $\text{Mn}_x\text{Ga}_{1-x}$  alloy films deposited on a Cr buffer layer. (a)  $x = 0.54$  and (b)  $x = 0.62$ .

ranging from 10 to 15  $\text{Merg}/\text{cm}^3$ . The  $K_u$  values for  $\text{Mn}_3\text{Ga}$  and  $\text{Mn}_2\text{Ga}$  alloys reported in Ref. 22 are larger than those in our films by a factor of 1.5–2.0, as shown in Fig. 5(b).

A significant change in the coercivity  $H_c$  is also observed along with increasing  $x$  values, as shown in Fig. 5(c). Thinner films show larger  $H_c$  values when compared with those of thicker films; this phenomenon is commonly observed in perpendicularly magnetized films. The large change in  $H_c$  can be ascribed to a large change in the values for  $H_k^{\text{eff}}$  against  $x$  (not shown here).

#### IV. DISCUSSION

In order to understand the composition dependence of  $M_S$ , we evaluated the magnetic moment  $m$  per unit cell for the alloy films, as shown in Fig. 6(a). The measured  $m$  values for the bulk Mn-Ga alloys<sup>14</sup> and for the epitaxial films of  $D0_{22}$   $\text{Mn}_2\text{Ga}$  and  $\text{Mn}_3\text{Ga}$ <sup>22</sup> are also shown in Fig. 6(a) for the purpose of comparison. The values of  $m$  in the previous reports are almost identical to those obtained by us for  $x$  values at around 0.70. Our  $m$  values are slightly larger than those estimated in the bulk alloy samples at  $x$  values of around 0.66 and smaller than the previous values obtained for  $\text{Mn}_2\text{Ga}$  films. In the following section, we discuss the origin of the linear reduction in magnetization against Mn composition.

As mentioned earlier, vacancies in the crystal structure of the alloy can be introduced when the Mn content is reduced in  $D0_{22}$   $\text{Mn}_3\text{Ga}$ . A Mn atom at the Wyckoff  $2b$  position ( $\text{Mn}_I$ ) has a local magnetic moment directed opposite to the net magnetic moment and the local magnetic moment of the  $\text{Mn}_{II}$  atom located at the Wyckoff  $4d$  position [Fig. 1(b)]; consequently, the Mn deficiencies at the  $2b$  sites tend to increase the value of  $m$ . The previous theoretical studies suggest that the values of  $m$  depend nonlinearly on the number of vacancies.<sup>14</sup> The

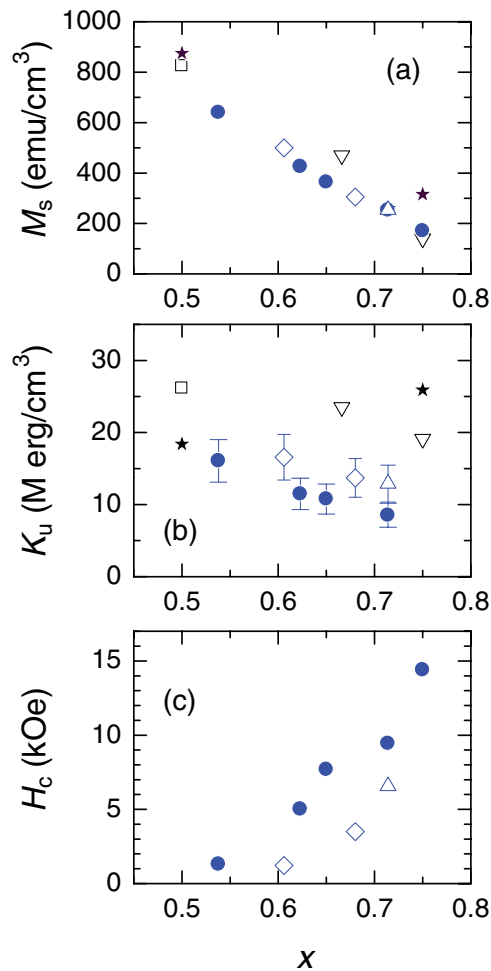


FIG. 5. (Color online) (a) Saturation magnetization  $M_s$ , (b) uniaxial magnetic anisotropy constant  $K_u$ , and (c) coercivity  $H_c$  as a function of composition  $x$  for  $\text{Mn}_x\text{Ga}_{1-x}$  alloy films with thicknesses of 30 nm ( $\bullet$ ) and 100 nm ( $\Delta$ ) deposited on a Cr buffer layer (Ref. 15) and with thickness of 100 nm deposited on MgO substrate ( $\diamond$ ) (Ref. 18). The values for  $H_c$  are obtained from hysteresis loops measured with the applied field aligned with the film normal. The measured values in Ref. 22 ( $\nabla$ ) and the calculated values in Ref. 30 ( $\square$ ) and this report ( $\star$ ) are plotted in (a) and (b).

theoretical  $m$  values obtained in Ref. 14 are also plotted in Fig. 6(a) with different distributions of vacancies. Here, model I corresponds to the calculation taking into account the Mn deficiencies only at the  $2b$  sites, and model II corresponds to the calculation with Mn deficiencies at both the  $2b$  and  $4d$  sites in a  $D0_{22}$   $\text{Mn}_3\text{Ga}$  unit cell [Fig. 1(b)].<sup>14</sup> Both models predict an increase in  $m$  with decreasing  $x$ , and the variation in  $m$  for model I is more pronounced than that in model II. The experimental  $m$  versus  $x$  curves shows a linear dependence, and it is different from the predicted values for both models, thereby indicating these models are not applicable to our films.

We can also consider an alternative model that does not introduce vacancies. As pointed out for  $L1_0$  Mn-Ga alloys,<sup>4</sup> a Mn atom can occupy the  $4d$  site preferentially to the  $2a$  and  $2b$  sites, in a manner similar to Mn atom behavior in  $\tau$  MnAl alloy. For  $x > 0.5$ , the extra Mn atom can replace the Ga atom at the  $2a$  or  $2b$  sites [Fig. 1(c)]. The local magnetic moment for

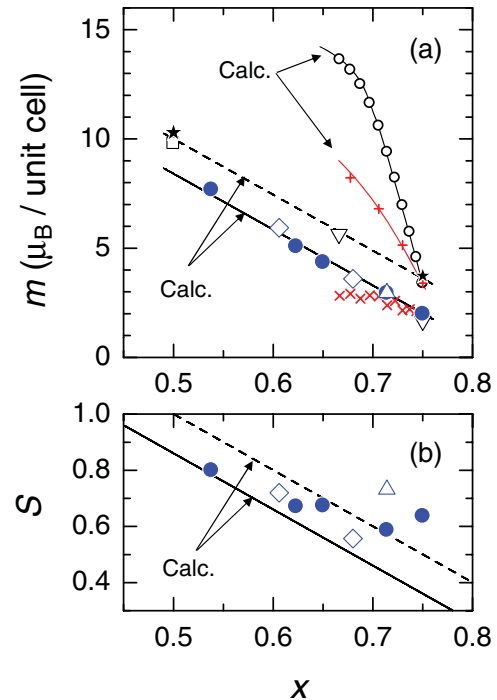


FIG. 6. (Color online) Composition dependence of (a) magnetic moment  $m$  per unit cell and (b)  $L1_0$  long-range ordering parameter  $S$  for  $\text{Mn}_x\text{Ga}_{1-x}$  alloy films with thickness of 30 nm ( $\bullet$ ) and 100 nm ( $\Delta$ ) deposited on a Cr buffer layer (Ref. 15) and with thickness of 100 nm deposited on a MgO substrate ( $\diamond$ ) (Ref. 18). The measured  $m$  values in Ref. 14 ( $\times$ ) and Ref. 22 ( $\nabla$ ) and the calculated  $m$  values in Ref. 30 ( $\square$ ) and in this report ( $\star$ ) are plotted in (a). The theoretical  $x$  dependencies of  $m$  are also shown for model I ( $\circ$ ) and model II ( $+$ ) (Ref. 14). The curves provide only a visual guide. The dashed and solid lines indicate the calculated  $m$  and  $S$  values with an occupation probability of Mn atoms at the Wyckoff  $4d$  position for  $p_{II} = 1.0$  and 0.93, respectively.

this extra Mn atom may couple antiferromagnetically to the magnetic moments of the Mn atoms at the  $4d$  sites, and this coupling could reduce the net magnetic moment for the Mn-Ga alloy. Here we assume that the local magnetic moment of the Mn atom is independent of both  $x$  and the atom's location at  $2a$  or  $2b$ , and the magnetic moment depends only on the location of the Mn atom at the sites  $4d$  or  $2a$  ( $2b$ ). The following simple relation expresses the theoretical magnetic moment per unit cell  $m$ :

$$m = 4(m_{II}p_{II} - |m_I|p_I). \quad (1)$$

Here,  $m_I$  ( $m_{II}$ ) and  $p_I$  ( $p_{II}$ ) denote the local magnetic moment and the occupation probability of a Mn atom at  $2a$  or  $2b$  ( $4d$ ) sites, respectively. The occupation probability obeys the following conservation law:

$$p_I + p_{II} = 2x. \quad (2)$$

From Eqs. (1) and (2),  $m$  is rewritten as

$$m = 4[(|m_I| + m_{II})p_{II} - 2|m_I|x]. \quad (3)$$

The values of  $m$  are calculated as a function of  $x$  using Eq. (3), and the resulting curve is shown in Fig. 6(a) for different  $p_{II}$

values. The experimental  $m$  value curve is reasonably fitted to the calculated values with  $p_{\parallel} = 0.93$  (solid line) if  $m_{\perp} = -3.2\mu_B$  and  $m_{\parallel} = 2.5\mu_B$  are used. These  $m_{\perp}$  and  $m_{\parallel}$  values are comparable with those evaluated in  $D0_{22}$   $Mn_3Ga$ <sup>13,14</sup> and  $L1_0$   $MnGa$ ,<sup>30</sup> and the values mentioned below. Interestingly, the values of  $m$  reported in the epitaxial  $Mn_2Ga$  film<sup>22</sup> lie on the line calculated with  $p_{\parallel} = 0$ , thereby possibly indicating that there may be negligible disorders in the film.

In order to verify the above possibility, the  $L1_0$  long-range ordering parameter  $S$  is estimated from the integrated intensity ratio of the (002) and (004) diffraction peaks in the XRD patterns for the alloy films using a standard method [Fig. 6(b)].<sup>31</sup> For this estimation, the Debye-Waller factor  $\sigma$  is set to 0.0156 (0.0104) nm for the  $L1_0$  ( $D0_{22}$ ) films; the value of this factor is obtained from the ratio of the (004) and (008) peak intensities for the 100-nm-thick films deposited on a MgO substrate. Theoretically,  $S$  is expressed as<sup>31</sup>

$$S = 2(p_{\parallel} - x). \quad (4)$$

The estimated value for  $S$  is plotted as a function of  $x$ , as shown by the dashed (solid) line for  $p_{\parallel} = 1.0$  (0.93) in Fig. 6(b). The maximum value for  $S$  is unity at  $x = 0.5$ ; subsequently,  $S$  decreases with increasing  $x$  (dashed line). The  $S$  value also reduces with decreasing  $p_{\parallel}$  values, i.e., due to the swapping of a Mn atom at the  $4d$  site with a Ga atom at the  $2a$  or  $2b$  sites. The experimental  $S$  value decreases with increasing  $x$ , and the ranges between the values for  $p_{\parallel} = 1.0$  and for 0.93 at  $0.5 < x < 0.7$  are roughly consistent with the value of  $p_{\parallel}$  used for the calculation of  $m$  in Fig. 6(a). The experimental  $S$  values are above the theoretical maxima at  $x > 0.7$ , thereby implying that the experimental  $S$  values are not reliable in this range. This might be due to an underestimation of the  $\sigma$  value for  $x > 0.7$ ; thus, microscopic characterization for atomic ordering is needed to confirm this model of localized magnetic moment.

In order to further discuss the validity of this picture, we calculated the electronic band structures of  $L1_0$   $MnGa$  and  $D0_{22}$   $Mn_3Ga$  using the lattice constants shown in Fig. 3(a). The resulting total and partial densities of states (DOSs) for  $L1_0$   $MnGa$  and  $D0_{22}$   $Mn_3Ga$  are shown in Figs. 7(a) and 7(b), respectively. The largest peak of the density of states in the minority (majority) spin band is located at an energy level greater (lesser) than the Fermi energy level in  $L1_0$   $MnGa$ , and this peak is chiefly attributed to the  $d$  orbitals of the Mn atoms at the  $Mn_{\parallel}$  sites. These peaks also appear for  $D0_{22}$   $Mn_3Ga$  even though finer structures appear owing to the  $D0_{22}$  superlattice [Fig. 7(b)], thereby implying that the magnetic moment of the Mn atoms at  $Mn_{\parallel}$  sites in  $D0_{22}$   $Mn_3Ga$  is not largely different from that for  $L1_0$   $MnGa$ . In fact, the magnetic moment of Mn at the  $Mn_{\parallel}$  site in  $D0_{22}$   $Mn_3Ga$  is estimated as  $2.5\mu_B$ , and this value is roughly identical to that for  $L1_0$   $MnGa$  ( $2.6\mu_B$ ). In  $D0_{22}$   $Mn_3Ga$ , there are a few fairly narrow peaks attributed to the  $d$  orbitals of the Mn atoms at the  $Mn_{\perp}$  sites, thereby indicating that these  $d$  orbitals are almost localized, and the resulting magnetic moment is estimated to be  $-3.1\mu_B$ . [The derived  $M_S$  values were also plotted in Fig. 5(a) for comparison.] This localized nature of  $d$  orbitals at  $Mn_{\perp}$  sites has also been observed in the context of Heusler alloys.<sup>32</sup> These physical insights gained from the electronic structures

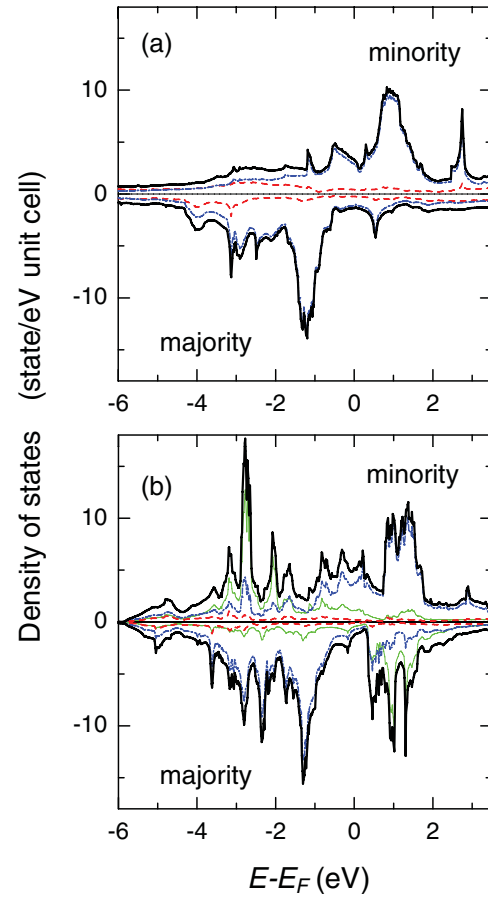


FIG. 7. (Color online) Spin-dependent total and partial densities of states (DOSs) in (a)  $L1_0$   $MnGa$  and (b)  $D0_{22}$   $Mn_3Ga$ . Total DOS is denoted by solid curves, and partial DOSs for  $Mn_{\perp}$ ,  $Mn_{\parallel}$ , and Ga are shown with thin solid, dot-dashed, and broken curves, respectively.

are in accord with the localized and composition-insensitive magnetic moment model suggested above.

The respective values of  $K_u$  calculated from first principles are also plotted in Fig. 5(b). The order of magnitude for the theoretical  $K_u$  values is in good agreement with those obtained in the experiment; however, the values for the  $D0_{22}$  phases are larger than those obtained in our experiments by a factor of 1.5–2.0. It is difficult to simultaneously interpret the data of  $K_u$  vs  $x$  on the basis of the speculated localized magnetic moment model. The orbital magnetic moments for the  $d$  ( $p$ ) orbitals of the Mn (Ga) atom, evaluated from the first-principles calculation including the spin-orbit interaction, are so small that we cannot explain the large  $K_u$  and its composition dependence. Further studies are required to obtain a unified physical picture that explains this composition dependence of  $M_S$  and  $K_u$  in Mn-Ga alloys. In addition, the studies need to utilize calculations from first principles to account for disorders.

## V. SUMMARY

In our study, we investigated the structural and magnetic properties of the  $Mn_xGa_{1-x}$  alloy films with different composition ratios. The  $M_S$  value was approximately  $600 \text{ emu/cm}^3$

at  $x = 0.54$ , and it reduced to approximately  $200 \text{ emu/cm}^3$  at  $x = 0.75$  while maintaining squared hysteresis curves and  $K_u$  values at around  $10\text{--}15 \text{ Merg/cm}^3$ . These data were analyzed using the localized magnetic moment model. The Mn-Ga alloy can be a promising material not only for STT-MRAM but also for other applications requiring materials with a high  $K_u$  value and widely tunable  $M_S$  values.

## ACKNOWLEDGMENTS

This work was partially supported by a Grant-in-Aid for Scientific Research from JSPS, the Strategic International Cooperative Program ASPIMATT from JST, and a Grant for Industrial Technology Research from NEDO, World Premier International Research Center Initiative (WPI) from MEXT, and the Casio foundation.

- 
- <sup>1</sup>D. Weller, A. Moser, L. Folks, M. E. Best, W. Lee, M. F. Toney, M. Schwickert, J.-U. Thiele, and M. F. Doerner, *IEEE Trans. Magn.* **36**, 10 (2000).
- <sup>2</sup>H. Yoda, T. Kishi, T. Nagase, M. Yoshikawa, K. Nishiyama, E. Kitagawa, T. Daibou, M. Amano, N. Shimomura, S. Takahashi, T. Kai, M. Nakayama, H. Aikawa, S. Ikegawa, M. Nagamine, J. Ozeki, S. Mizukami, M. Oogane, Y. Ando, S. Yuasa, K. Yakushiji, H. Kubota, Y. Suzuki, Y. Nakatani, T. Miyazaki, and K. Ando, *Curr. Appl. Phys.* **10**, e87 (2010).
- <sup>3</sup>S. Ikeda, K. Miura, H. Yamamoto, K. Mizunuma, H. D. Gan, M. Endo, S. Kanai, J. Hayakawa, F. Matsukura, and H. Ohno, *Nature Mater.* **9**, 721 (2010).
- <sup>4</sup>T. A. Bither and W. H. Cloud, *J. Appl. Phys.* **36**, 1501 (1965).
- <sup>5</sup>K. M. Krishnan, *Appl. Phys. Lett.* **61**, 2365 (1992).
- <sup>6</sup>M. Tanaka, J. P. Harbison, J. DeBoeck, T. Sands, B. Phillips, T. L. Cheeks, and V. G. Keramidis, *Appl. Phys. Lett.* **62**, 1565 (1993).
- <sup>7</sup>C. Adelmann, J. L. Hilton, B. D. Schlutz, S. McKernan, C. J. Palmstrom, X. Lou, H.-S. Chiang, and P. A. Crowell, *Appl. Phys. Lett.* **89**, 112511 (2006).
- <sup>8</sup>E. Lu, D. C. Ingram, A. R. Smith, J. W. Knepper, and F. Y. Yang, *Phys. Rev. Lett.* **97**, 146101 (2006).
- <sup>9</sup>E. Krén and G. Kádér, *Solid State Commun.* **8**, 1653 (1970).
- <sup>10</sup>H. Niida, T. Hori, H. Onodera, Y. Yamaguchi, and Y. Nakagawa, *J. Appl. Phys.* **79**, 5946 (1996).
- <sup>11</sup>S. Wurmehl, H. C. Kandpal, G. H. Fecher, and C. Felser, *J. Phys. Condens. Matter* **18**, 6171 (2006).
- <sup>12</sup>J. Kubler, *J. Phys. Condens. Matter* **18**, 9795 (2006).
- <sup>13</sup>B. Balke, G. H. Fecher, J. Winterlik, and C. Felser, *Appl. Phys. Lett.* **90**, 152504 (2007).
- <sup>14</sup>J. Winterlik, B. Balke, G. H. Fecher, C. Felser, M. C. M. Alves, F. Bernardi, and J. Morais, *Phys. Rev. B* **77**, 054406 (2008).
- <sup>15</sup>F. Wu, S. Mizukami, D. Watanabe, H. Naganuma, M. Oogane, Y. Ando, and T. Miyazaki, *Appl. Phys. Lett.* **94**, 122503 (2009).
- <sup>16</sup>F. Wu, E. P. Sajitha, S. Mizukami, D. Watanabe, H. Naganuma, M. Oogane, Y. Ando, and T. Miyazaki, *Appl. Phys. Lett.* **96**, 042505 (2010).
- <sup>17</sup>F. Wu, S. Mizukami, D. Watanabe, E. P. Sajitha, H. Naganuma, M. Oogane, Y. Ando, and T. Miyazaki, *IEEE Trans. Magn.* **46**, 1863 (2010).
- <sup>18</sup>S. Mizukami, F. Wu, A. Sakuma, J. Walowski, D. Watanabe, T. Kubota, X. Zhang, H. Naganuma, M. Oogane, Y. Ando, and T. Miyazaki, *Phys. Rev. Lett.* **106**, 117201 (2011).
- <sup>19</sup>T. Kubota, Y. Miura, D. Watanabe, S. Mizukami, F. Wu, H. Naganuma, X. Zhang, M. Oogane, M. Shirai, Y. Ando, and T. Miyazaki, *Appl. Phys. Express* **4**, 043002 (2011).
- <sup>20</sup>T. Kubota, S. Mizukami, D. Watanabe, F. Wu, X. Zhang, H. Naganuma, M. Oogane, Y. Ando, and T. Miyazaki, *J. Appl. Phys.* **110**, 013915 (2011).
- <sup>21</sup>H. Kurt, K. Rode, M. Venkatesan, P. S. Stamenov, and J. M. D. Coey, *Phys. Rev. B* **83**, 020405 (2011).
- <sup>22</sup>H. Kurt, K. Rode, M. Venkatesan, P. Stamenov, and J. M. D. Coey, *Phys. Status Solidi B* **248**, 2338 (2011).
- <sup>23</sup>C. L. Zha, R. K. Dumas, J. W. Lau, S. M. Mohseni, S. R. Sani, I. V. Golosovsky, A. F. Monsen, J. Nogue, and J. Akerman, *J. Appl. Phys.* **110**, 093902 (2011).
- <sup>24</sup>K. Wang, A. Chinchore, W. Lin, D. C. Ingram, A. R. Smith, A. J. Hauser, and F. Yang, *J. Cryst. Growth* **311**, 2265 (2009).
- <sup>25</sup>W. Feng, D. V. Thiet, D. D. Dung, Y. Shin, and S. Cho, *J. Appl. Phys.* **108**, 113903 (2010).
- <sup>26</sup>A. Bedoya-Pinto, C. Zube, J. Malindretos, A. Urban, and A. Rizzi, *Phys. Rev. B* **84**, 104424 (2011).
- <sup>27</sup>K. Wang, E. Lu, J. W. Knepper, F. Yang, and A. R. Smith, *Appl. Phys. Lett.* **98**, 162507 (2011).
- <sup>28</sup>T. Kubota, M. Araidai, S. Mizukami, X. Zhang, Q. Ma, H. Naganuma, M. Oogane, Y. Ando, M. Tsukada, and T. Miyazaki, *Appl. Phys. Lett.* **99**, 192509 (2011).
- <sup>29</sup>A. Sakuma, *J. Phys. Soc. Jpn.* **63**, 1422 (1994).
- <sup>30</sup>A. Sakuma, *J. Magn. Mater.* **187**, 105 (1998).
- <sup>31</sup>K. Barmak, J. Kim, L. H. Lewis, K. R. Coffey, M. F. Toney, A. J. Kellock, and J.-U. Thiele, *J. Appl. Phys.* **98**, 033904 (2005).
- <sup>32</sup>T. Graf, C. Felser, and S. S. P. Parkin, *Prog. Solid State Chem.* **39**, 1 (2011).